

Broadband Anomalous Reflection with Dispersion Controlled Metasurfaces

Ashif A. Fathnan,¹ Andreas E. Olk,^{1,2} and David A. Powell¹

¹*School of Engineering and Information Technology,
University of New South Wales (UNSW) Canberra, Australia**

²*IEE S.A., 1, rue de Campus, 7795 Bissen, Luxembourg*

(Dated: July 19, 2022)

Metasurfaces have emerged as a promising technology for the manipulation of electromagnetic waves within a thin layer. Initially based on narrowband design principles, the field has since expanded to include broadband achromatic designs, which maintain reflection or refraction angles over some bandwidth, and broadband dispersive designs, which maintain high efficiency in a broad bandwidth, but with varying reflection or refraction angle. To date most of these broadband structures were designed using relatively ad-hoc methods. For planar metallic structures used at microwave and millimeter waves, there exist rigorous narrowband design methods, based on the equivalent impedance of the patterned metallic layers. In this work we extend these methods, to show how broadband impedance functions can be fitted to LC resonance models. This enables the realization of broadband reflective metasurfaces, using relatively simple geometries. We show the limitations on bandwidth that arise when using a structure with a single resonance, and the minimum physically realizable frequency, which is dictated by the substrate properties. We demonstrate that for achromatic metasurfaces, the required capacitance and inductance values become extreme as the metasurface size increases, leading to difficulties in realizing them with meta-atoms. Therefore, we apply our method to the design and realization of a broadband dispersive metasurface, which avoids extreme values. We perform measurements at millimeter wave frequencies, showing a fractional bandwidth of 18.22%, compared to 9.98% for a reference design based on the more conventional narrowband approach.

I. INTRODUCTION

Metasurfaces are a unique type of metamaterial, where control of propagating waves can be achieved with thin layers of scattering elements. Metasurfaces enable wave-front control by introducing abrupt changes in radiation properties, rather than through continuous changes of permittivity or permeability within a bulk metamaterial. Using this simple concept, metasurfaces have enabled various wave phenomena such as anomalous refraction or reflection [1–4], focusing [5–7], vortex beam generation [8, 9] and coupling of surface and plane waves [10, 11]. For microwave and millimeter wave structures based on patterned metallic layers, the use of equivalent surface impedances enables robust design methods which can realize essentially arbitrary wavefront manipulation functions [12, 13].

Typically a resonant response is exploited in metasurfaces to introduce an abrupt phase change of the radiating wave over the full 2π range. By detuning individual elements (known as meta-atoms) to engineer their phase shift (or equivalently, their surface impedance), efficient wavefront control can be achieved, but it is often limited to a narrow bandwidth around the design frequency. In addition to the bandwidth limits imposed by using resonant elements, the impedance profile of a metasurface is typically divided into a number of Fresnel zones [14], leading to a diffractive structures with strong angular dependence on frequency, causing distortion of the wave-front known as chromatic aberration.

Techniques to overcome the bandwidth limitations of metasurfaces can be divided into three broad classes. The first is to

create a metasurface which operates at multiple discrete wavelengths, by spatially-multiplexing different sized resonators [15, 16]. This approach has been shown to be effective, but it is limited to applications where only specific narrow bands are of interest, such as optical displays. A second approach, which we term broadband dispersive design, is to allow the reflection or refraction angle to vary with frequency, while ensuring that specular reflection and unwanted diffraction orders are suppressed over a significant bandwidth. This has been achieved using trapezoidal metallic elements [17, 18], rectangular sub-wavelength nanobricks [4, 6], stub-loaded metallic patches [19] or complex shaped all-dielectric structures [20].

The third approach to improving the operating bandwidth of metasurfaces is broadband achromatic designs, which maintain fixed reflection or refraction angle over their operating bandwidth. In addition to controlling the phase delay, in these structures the designers engineer group delay [21], i.e. the derivative of phase with respect to frequency. Achromatic metasurfaces have been realized using dielectric phase shifting structures [22, 23], a combination of Pancharatnam-Berry phase with gap-plasmons [24] or dielectric resonators [25], two layers of metallic ring resonators [26], and multiple layers of non-resonant metallic elements [27]. Although these metasurfaces demonstrated achromatic operation, achieving the required variation in group delay across the metasurface requires non-periodic structures. The structural complexity of such non-periodic metasurfaces increases with their size, hence they are limited to relatively small aperture sizes [28]. Additionally, the increasing complexity can be problematic especially when fabrication limits comes into play, such as in the millimeter-wave regime where there is a minimum feature size associated with printed circuit board (PCB) manufacturing techniques [29].

In this paper, we present a more insightful analytical ap-

* a.fathnan@student.unsw.edu.au

proach to obtain broadband operation of a metasurface. We extend the surface impedance models, to show how broadband operation can be systematically implemented using LC resonant elements in a metasurface containing only a single patterned metal layer. We apply this approach for anomalous reflection, where the metasurface is designed to reflect all incoming energy into a single, non-specular direction. The impedance of the metasurface is adjusted to control the group delay across its surface, obtaining both broadband dispersive and achromatic designs. For achromatic metasurfaces, the LC resonant meta-atoms are non-periodic, with more extreme values required as the metasurface size increases. We show that these extreme values make the achromatic design unfeasible for fabrication at millimeter wave frequencies, so we realize only the broadband dispersive design. For benchmarking purposes, we also consider a metasurface designed using the conventional narrowband synthesis approach. Both the broadband dispersive and narrowband metasurfaces are designed for operation in the W-band (75-110 GHz). The structures are fabricated using a commercial PCB fabrication process, and far-field angle-resolved measurements are used to verify the superior performance of the broadband dispersive metasurface.

II. DESIGN OF BROADBAND METASURFACE FOR ANOMALOUS REFLECTION

A. Achromatic and Dispersive Metasurface Designs

Here we consider an anomalous reflection problem with a metasurface having one patterned metallic layer, separated from a metallic ground plane by a dielectric substrate, as shown in Fig. 1(a). The incident beam impinging upon the metasurface at an angle of θ_i and reflected at an angle of θ_o

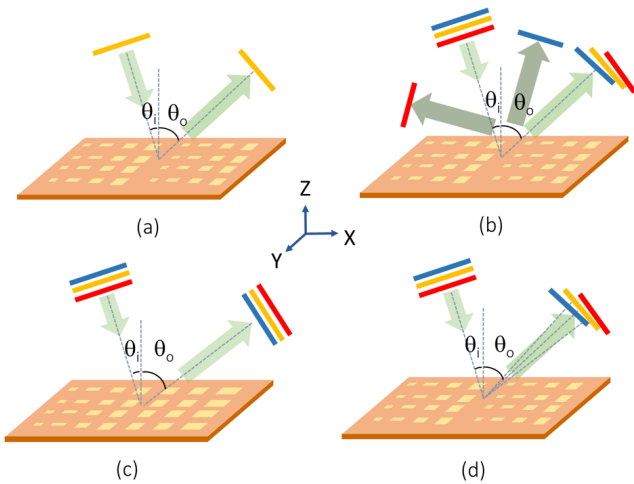


FIG. 1. Metasurface performing anomalous reflection under different scenarios: (a) narrowband design with narrowband illumination, (b) narrowband design with broadband illumination, (c) broadband achromatic design (constant angle responses), (d) broadband dispersive design (frequency dependent angle).

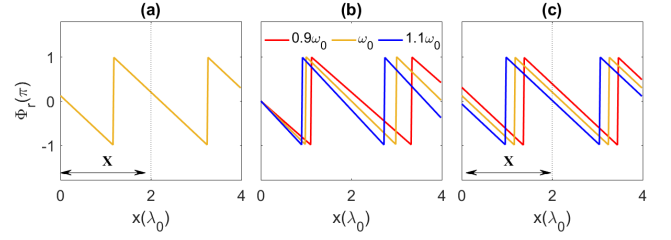


FIG. 2. Phase profile of metasurface: (a) narrowband design, (b) broadband achromatic design, (c) broadband dispersive design.

requires the metasurface to provide a phase discontinuity Φ_r while maintaining high reflection amplitude. The phase Φ_r changes linearly with respect to position x across the metasurface and frequency ω , and is formulated as [30],

$$\Phi_r(x, \omega) = \omega x (\sin \theta_{\text{out}} - \sin \theta_{\text{in}}) / c + \Phi_0(\omega) \quad (1)$$

Here, c is the speed of light in vacuum and $\Phi_0(\omega)$ is an arbitrary additional phase term independent of x , which does not affect the reflection angle. The corresponding phase profile along x is shown in Fig. 2(a). Considering a metasurface designed only to operate at center frequency ω_0 , degradation is inevitable as the working frequency shifts further away from the design frequency. As illustrated in Fig. 1(b), at other frequencies, spurious diffraction orders are excited (dark green arrows), reducing the metasurface efficiency in broadband operation.

In the design of a broadband achromatic metasurface, in addition to a center frequency of ω_0 , a certain fractional bandwidth ($\Delta\omega$) is chosen. As illustrated by Fig. 1(c), a broadband incident beam is reflected into the same angle at all frequencies. This operation requires the metasurface to have a distinct phase profile for every frequency within its bandwidth of interest, as shown in Fig. 2(b). Therefore, broadband achromatic metasurfaces require a non-periodic structure and become increasingly difficult to realize for large bandwidths and aperture sizes [28].

Alternatively, broadband metasurfaces can be designed to direct energy into a chosen diffraction order with high efficiency over some broad band. The diffraction order in this case however corresponds to a frequency-dependent reflection angle, as shown in Fig. 1(d). In particular, using this approach, the metasurface is designed to satisfy Eq. (1) for the desired angle at a chosen center frequency $\omega_0 = 2\pi f_0$, and maintain the same phase profile over the desired bandwidth $\Delta\omega$. This leads to a periodic reflection phase, with period X given by

$$X = \frac{\lambda_0}{\sin \theta_{\text{out}} - \sin \theta_{\text{in}}}, \quad (2)$$

where $\lambda_0 = f_0/c$. Due to the fact that the periodicity simplifies the design, the reflection angle is however not exactly constant over frequency, this alternative approach can be considered as compromise between performance and complexity. We will refer to this approach as the broadband dispersive design. The

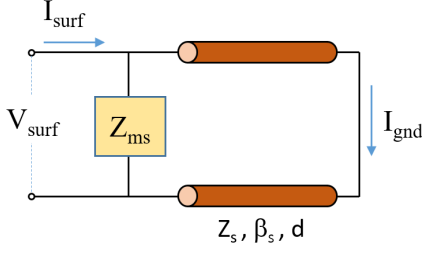


FIG. 3. Equivalent circuit of each unit cell of the metasurface.

reflection phase can then be expressed as

$$\Phi_r(x, \omega) = 2\pi \frac{x}{X} + \Phi_0(\omega) \quad (3)$$

This local reflection phase profile is shown in Fig. 2(c). We see that the required phase profile is no longer dependent upon frequency, except for the additional linear phase term Φ_0 . The group delay imparted by the phase profile is constant across all positions and only depends on the choice of Φ_0 . The effect of this group delay on the metasurface realizability will be shown in Section II C.

B. Surface Impedance Model

The broadband phase response given in Eqs. (1) and (3) is based on geometric optics. More physical insight can be obtained in terms of surface impedance distribution, i.e. the ratio of electric and magnetic field components tangential to the metasurface. The relationship between reflection phase and surface impedance is stipulated as [12]:

$$Z_{\text{surf}}(x, \omega) = -jZ_o \cot(\Phi_r/2) \quad (4)$$

The required surface impedance of the metasurface is purely imaginary and is proportional to the output impedance ($Z_o = \eta / \cos \theta_o$) with a cotangent function of phase $\phi_r/2$. Here, η refers to the free space impedance.

It has been shown that this solution leads to spurious diffraction in cases where the difference between θ_{out} and θ_{in} is large [13], due to its inability to simultaneously impedance match both the incident and reflected waves. However, the efficiency of diffraction into the desired order can still be close to unity if the reflection angle is below 40° . Moreover, using the above equation, an equivalent circuit can be introduced to obtain the required impedance of the metasurface, facilitating the unit-cell design process. Here, as shown in Fig. 3, each meta-atom is described as a shunt impedance Z_{ms} loading a transmission line, which represents propagation through a dielectric substrate of thickness d . The other port of the transmission line is grounded [31], representing the metallic ground plane. Based on this equivalent circuit, the surface impedance Z_{surf} is expressed as the ratio between the equivalent surface voltage (V_{surf}) and current (I_{surf}). By representing the meta-atom layer by its admittance $Y_{\text{ms}} = Z_{\text{ms}}^{-1}$, and representing the transmission line via its ABCD transfer param-

eters, we can relate the surface voltages and currents to those on the ground plane as

$$\begin{bmatrix} V_{\text{surf}} \\ I_{\text{surf}} \end{bmatrix} = \begin{bmatrix} 1 & 0 \\ Y_{\text{ms}} & 1 \end{bmatrix} \begin{bmatrix} A & B \\ C & D \end{bmatrix} \begin{bmatrix} 0 \\ I_{\text{gnd}} \end{bmatrix}. \quad (5)$$

This enables us to relate the required value of Z_{surf} to other parameters in the circuit as

$$Z_{\text{surf}} = \frac{V_{\text{surf}}}{I_{\text{surf}}} = \frac{B}{Y_{\text{ms}}B + D}, \quad (6)$$

where the unknown current I_{gnd} cancels out. We assume that the substrate thickness d , permeability μ_s and permittivity ϵ_s are specified, based on the properties of available materials. This enables us to substitute the transmission line parameters $B = jZ_s \sin(\beta_s d)$ and $D = \cos(\beta_s d)$ into Eq. (6), where the substrate wavenumber is $\beta_s = \omega \sqrt{\mu_0 \epsilon_0 \epsilon_s}$ and its impedance is $Z_s = \sqrt{\frac{\mu_0}{\epsilon_0 \epsilon_s}} = \frac{\eta}{\sqrt{\epsilon_s}}$, and ϵ_0 and μ_0 are free space permittivity and permeability. We can then solve for the required impedance Z_{ms} of the meta-atom layer as

$$Z_{\text{ms}} = \frac{1}{Y_{\text{ms}}} = \frac{jZ_{\text{surf}}Z_s \tan(\beta_s d)}{jZ_s \tan(\beta_s d) - Z_{\text{surf}}}. \quad (7)$$

This solution yields the impedance requirement for each meta-atom in order to diffract energy into the desired angle. The purely imaginary impedance given by Eq. (7) can also be extended over a certain bandwidth of interest, to obtain a broadband metasurface. In Fig. 4(a) and (b), we plot the reactance $X_{\text{ms}} = \text{imag}(Z_{\text{ms}})$ as a function of both frequency and position, with an additional group delay of $t_0 = 17.5$ ps (see Section II C). We see that the broadband achromatic design yields a reactance which is non-periodic, whereas the broadband dispersive design yields a periodic reactance. In Fig. 4(c), considering a certain bandwidth over which the metasurface should be achromatic, the required number of resonators increases with the distance x from the center of the metasurface, indicated by the increasing number of poles and zeros. This is consistent with previous works on achromatic metasurfaces [23, 24, 26], in which the required number of resonators in meta-atoms increases with the metasurface size Δx . In contrast, for the dispersive design where the reflection angle varies with frequency, as shown by Fig. 4(d), the number of poles and zeros in the operating band remains constant, and they are spaced periodically in both position and frequency. It is important to note that although the original impedance formula requires Z_o to be dependent upon variation of θ_{out} , here we use a constant Z_o which is valid for the center operational frequency f_0 , and this has a minimal effect on the meta-atom layer impedance Z_{ms} as will be shown in Section II D.

C. Group Delay and Realizability of Impedances

As outlined in Section I, controlling the variation of group delay $t_g = d\Phi_r/d\omega$ across the metasurface is required for both broadband dispersive and achromatic operation. Although the

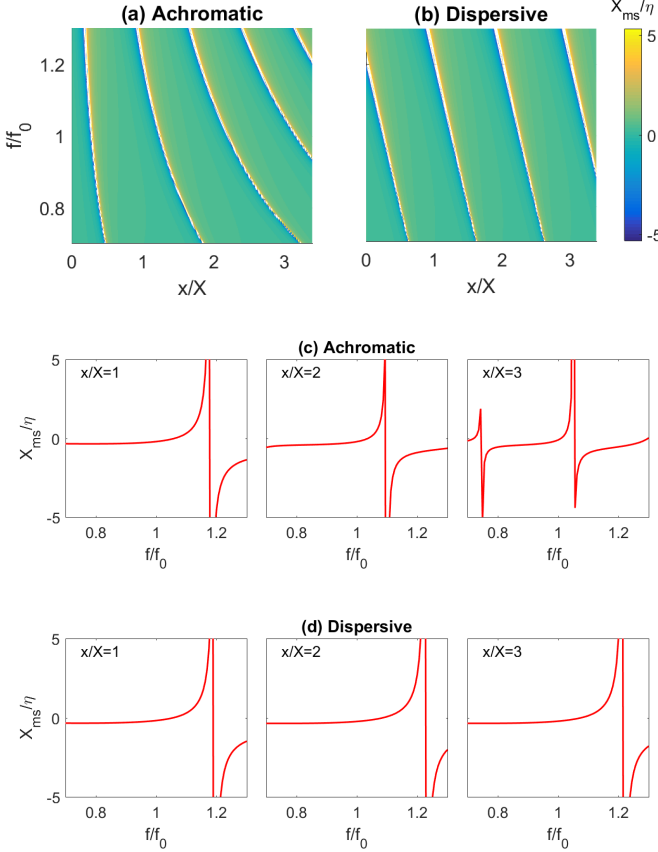


FIG. 4. The required meta-atom layer impedance as a function of both frequency f and position x for (a) broadband achromatic, and (b) broadband dispersive designs. The required meta-atom layer impedance as a function of frequency for selected positions x for (c) broadband achromatic, and (d) broadband dispersive designs. $X = 7.8\text{mm}$ is the period of metasurface for the center frequency $f_0 = 80\text{GHz}$, with the designed anomalous reflection angle $\theta_{\text{out}} = 30^\circ$ and normally incident illumination. The substrate is 0.254mm thick with a relative permittivity of 3.

group delay has both a position dependent part, and a contribution from the additional phase Φ_0 , most of the discussion in the literature has been dedicated to the first part. In most works, the additional phase has been included in the metasurface design, but merely as a free adjustment parameter. This parameter has been used, for example, to tailor the required phase profile over a frequency range [25, 32], or to reduce extreme values of metasurface impedance so that they can be realized by meta-atoms [33]. The effect of the additional phase Φ_0 on the metasurface bandwidth and realizability has not been investigated in depth. Here, we systematically show that the choice of Φ_0 affects metasurface bandwidth and realizability, and it serves as an important parameter for optimizing broadband operation.

Consider the broadband dispersive metasurface design in which its phase profile is stipulated by Eq. (3). Here, the phase imparted by the meta-atom's position is independent of frequency, so the additional phase $\Phi_0(\omega)$ completely determines

the group delay. The additional group delay is represented as t_0 and the extra phase term is linear in frequency to avoid group delay dispersion, i.e. $\Phi_0 = \omega t_0$. The reflection phase given by Eq. (3) can then be re-written as

$$\Phi_r = \frac{2\pi x}{X} + \omega t_0. \quad (8)$$

For the achromatic case, the group delay is determined by position dependent phase and the additional phase Φ_0 . The reflection phase given by Eq. (1) can then be re-written as

$$\Phi_r = \omega \left(\frac{\Delta\theta x}{c} + t_0 \right), \quad (9)$$

where $\Delta\theta = \sin\theta_{\text{out}} - \sin\theta_{\text{in}}$. As we will show below, the required additional group delay t_0 is partly determined by the delay the wave experiences propagating through the substrate. Accordingly, we can express the effect of propagation through the substrate as a time delay t_s . This amounts to replacing the term $\beta_s d$ in Eq. (7), with ωt_s , where $t_s = \sqrt{\epsilon_s} d/c$ is the time for a single pass through the substrate of thickness d . We substitute Eq. (4) to Eq. (7) and the required meta-atom layer impedance can be written as

$$Z_{ms} = \frac{Z_o Z_s \tan(\omega t_s) \cot(\Phi_r/2)}{j Z_s \tan(\omega t_s) + j Z_o \cot(\Phi_r/2)}. \quad (10)$$

In Eq. (10), an achromatic or dispersive metasurface is implemented by choosing the corresponding Φ_r from Eq. (8) or (9). In both cases, the group delay t_0 serves as a complementary design parameter, enabling the metasurface impedance variation with frequency and position to be conditioned. Fig. 5(a) and (b) show how the metasurface impedance Z_{ms} varies with both position and frequency, for different values of group delay from 10 to 25 ps. The left column shows the broadband dispersive case and the right column shows the achromatic case. Here, the metasurface design parameters are similar to those in Section II B. In Fig. 5(e) and (f) we consider the frequency dependent impedance at a particular position $x=4.8\text{mm}$ ($x/X = 0.6$). As the group delay increases, the impedance variation with frequency becomes stronger, causing more zeros and poles to occur within any chosen frequency range.

For the common case that each element of the metasurface is designed only to exhibit a single resonance, the increasing delay leads to a smaller operating bandwidth. From Fig. 5(e) and (f) we see that an upper bound on the bandwidth achievable with a single resonance (Δf) can be obtained from the frequency spacing between zeros (indicated by circles) and the mid-point between two zeros (indicated by crosses). This bandwidth can be expressed analytically by finding the location of zeros of Z_{ms} from Eq. (10). For reasonable substrate thickness values, the zeros of $\tan(\omega t_s)$ will occur at very high frequency, thus the zeros of $\cot(\Phi_r/2)$ are of interest. Solving for these zeros for the dispersive case yields

$$\omega_{z,m} = \frac{\pi + 2m\pi - \frac{2\pi x}{X}}{t_0}, \quad (11)$$

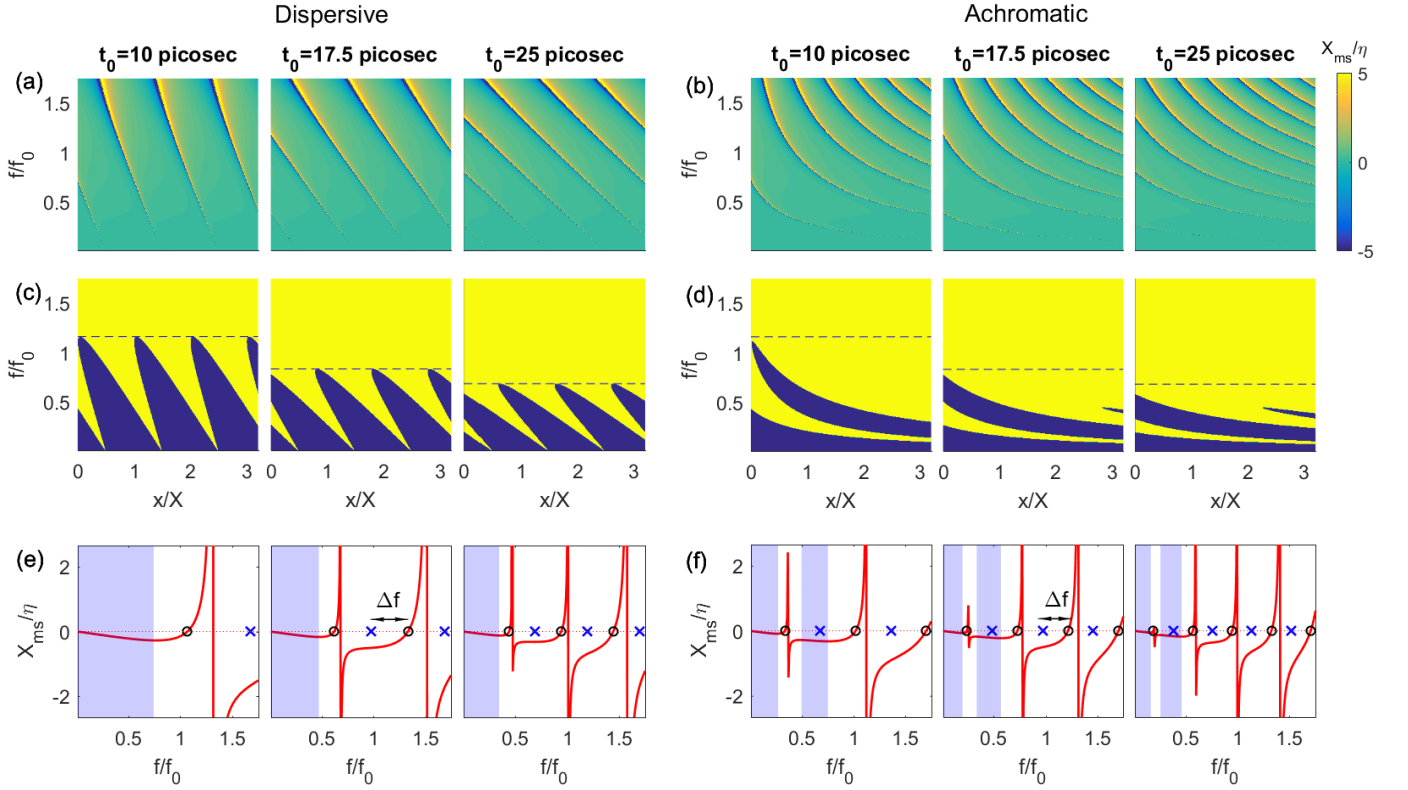


FIG. 5. Effect of group delay variation in dispersive and achromatic metasurface on: (a)-(b) Normalized meta-atom layer impedance as a function of both frequency and position. (c)-(d) Realizability of impedance with a passive lossless metasurface (blue color indicates non-realizable, yellow color indicates realizable, dashed lines indicate f_m , the minimum usable frequency). (e)-(f) Frequency-dependent impedance at $x=4.8$ mm ($x/X = 0.6$). Blue shading indicates non-realizable impedance with negative slope i.e. $dX_{ms}/d\omega \leq 0$. Circles indicate the location of zeros, and crosses indicate the centre position between two zeros. A one resonator bandwidth (Δf) is defined as frequency difference between circles and crosses.

where m is an arbitrary integer. For the achromatic case, the zeros are located at

$$\omega_{z,m} = \frac{\pi + 2m\pi}{t_0 + \Delta\theta\Delta x/c} \quad (12)$$

Given the strong dispersion of the impedance functions near the poles, we consider that a reasonable upper limit on the achievable bandwidth is half the difference between adjacent zeros, i.e. $\Delta f = \frac{1}{4\pi}(\omega_{z,m+1} - \omega_{z,m})$. This quantity is independent of m , and has the following expressions:

$$\Delta f = \frac{1}{2t_0} \quad (\text{Dispersive}), \quad (13)$$

$$\Delta f = \frac{1}{2(t_0 + \Delta\theta\Delta x/c)} \quad (\text{Achromatic}). \quad (14)$$

Here, $\Delta x = x_{\max} - x_{\min}$ is the width of the metasurface, which only affects the bandwidth in the achromatic case. In Fig. 6(a), we plot this maximum bandwidth as a function of group delay, for a realistic metasurface width of 23.4 mm or three times the period of the dispersive case ($\Delta x=3X$). It can be seen that a lower group delay allows a single resonance structure to achieve larger operational bandwidth. Moreover, the bandwidth in the achromatic case is smaller than the dispersive case for all values of the additional group delay t_0 , due

to the increasing number of resonances required at the larger values of x . Equation (13) suggests that a very high bandwidth could be achieved for a dispersive metasurface based on a single resonance structure, by choosing a small value of t_0 . Therefore, it is necessary to understand the constraints on the choice of t_0 .

A key consideration in choosing the additional group delay t_0 is whether the required reactance can be realized by a

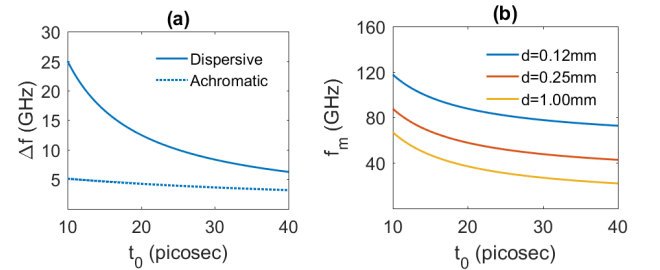


FIG. 6. (a) Bandwidth of one resonator versus group delay. (b) Minimum frequency operation for passive realization versus group delay in the broadband dispersive metasurface with respect to a variation of substrate thickness.

passive lossless metasurface. According to Foster's reactance theorem [34], the reactance must be monotonically increasing with frequency ($\frac{d}{d\omega}X_{\text{ms}} \geq 0$) to comply with passivity and causality limitations. It can be seen from Fig. 5(e) and (f) that there is a low frequency region where the reactance decreases with frequency, shaded in blue. In this frequency region, a passive implementation cannot be lossless and still exhibit the required frequency dispersion. The transition from negative to positive derivative of reactance marks the boundary between the Foster and non-Foster region, and can be obtained by finding the zeros of the frequency derivative of Z_{ms} , i.e.

$$\frac{dZ_{\text{ms}}}{d\omega} = 0. \quad (15)$$

We apply this derivative operation to Eq. (10) as detailed in Appendix A, and the result for the dispersive case is

$$\frac{2Z_o}{t_0} \cos^2\left(\frac{\pi x}{X} + \frac{\omega t_0}{2}\right) = \frac{Z_s}{t_s} \sin^2(\omega t_s) \quad (16)$$

For the achromatic case, the result is

$$\frac{2Z_o}{\left(\frac{\Delta\theta x}{c} + t_0\right)} \cos^2\left(\frac{\omega\Delta\theta x}{2c} + \frac{\omega t_0}{2}\right) = \frac{Z_s}{t_s} \sin^2(\omega t_s). \quad (17)$$

We see that the left hand sides of Eqs. (16) and (17) contain quantities that depend on the refraction angle (Z_o , X , $\Delta\theta$) and position x , as well as the additional group delay t_0 . The right hand sides contain quantities which depend only on the substrate properties. In Fig. 5(c) and (d), the frequency derivative of the reactance is plotted as a function of frequency and position. The Foster compliant region is shaded in yellow, and the non-Foster region is shaded in blue. The boundary between these two regions is given by Eq. (15). It can be seen that this realizability condition varies with position x across the metasurface. For realization of the structure, we need to find the minimum frequency f_m , where all elements are realizable, indicated by the dashed line in Fig. 5(c) and (d).

Inspecting Eq. (16), for a dispersive metasurface, we note that the term $\cos^2\left(\frac{\pi x}{X} + \frac{\omega t_0}{2}\right)$ varies between 0 and 1 for any value of ω . Therefore, we set this term to its maximum value of 1, which leads to the following upper bound solution for f_m .

$$f_m = \frac{1}{2\pi t_s} \arcsin\left(\sqrt{\frac{2Z_o t_s}{Z_s t_0}}\right). \quad (18)$$

For the achromatic case, we note that the upper bound solution of f_m occurs at $x = 0$. Applying this to Eq. (17), the left hand side becomes similar to the dispersive case of Eq. (16). Therefore, the limit given by Eq. (18) also applies to the achromatic case, although as can be seen from Fig. 5(d), the limit is slightly conservative for this case.

As the minimum frequency where the metasurface can be realized (f_m) depends on the additional group delay t_0 , this parameter must be chosen consistently with all other design parameters, particularly the substrate delay t_s . Fig. 6(b) shows how f_m varies with t_0 , for different choices of substrate thickness d (which determines t_s). It can be seen that for thinner

substrates, the minimum frequency f_m is increased. This gives us an important insight that a broadband metasurface *cannot be infinitesimally thin*, since it will cause the minimum realizable frequency f_m to be extremely high. On the other hand, increasing the substrate time delay, either by increasing the substrate thickness or dielectric constant, can be used to reduce the realizable operating frequency. Note that from Eq. (13) and (14), the bandwidth (Δf) can always be enlarged by reducing the additional group delay, and from Fig. 6(b) we see that thicker substrates permit lower values of t_0 . Therefore, increasing the substrate thickness effectively increases the operating bandwidth, in line with several works reported in the literature. For example, in thin microstrip antennas, a common method to increase the bandwidth is to choose a larger substrate thickness [35, 36]. Increasing the substrate thickness has also been reported to increase the bandwidth of a metasurface. For example in [37], increasing the substrate thickness detuned two metallic nano-rod resonances, allowing a more broadband phase responses in transmission operation.

D. Realization of Broadband Impedance

Having determined the meta-atom layer impedance profile for broadband operation, it is required to translate the abstract impedance functions into realistic metallic structures. Several works on transmissive Huygens' metasurfaces [33, 38] have shown this impedance translation procedure, however, they rely heavily on numerical tools and consider only narrowband operation. To efficiently realize a broadband metasurface, a more general approach for fitting the impedance over a broad frequency range is required.

From the required meta-atom layer impedances Z_{ms} , we see that structures exhibiting poles or zeros of the impedance, can be used for implementing anomalous reflection over a broad bandwidth. As shown in Fig. 4(b), if we choose a certain center frequency f_0 and set a limited operational bandwidth, the impedance Z_{ms} may have poles or zeros within the operating bandwidth. The number of resonances within the bandwidth can be more than one, however, we keep one LC resonance to fit the impedance Z_{ms} to minimize the design complexity. In cases where Z_{ms} has a zero within the operating bandwidth, a series LC resonance configuration is fitted to the required impedance. Whereas in cases where Z_{ms} has a pole within the operating bandwidth, the impedance is fitted with a parallel LC resonance.

To facilitate the design of realistic structures, we find the series inductance (L_s) and capacitance (C_s) required for the LC-series implementation. The general solution for the LC-series reactance is

$$X(\omega_0) = \omega_0 L_s - \frac{1}{\omega_0 C_s} \quad (19)$$

$X(\omega_0)$ is the imaginary part of impedance at the center frequency (ω_0) stipulated by Eq. (7). To obtain a solution for two variables (L_s and C_s) an additional equation is needed. From Eq. 19 we can calculate the derivative of the reactance at ω_0 ,

which can be related to the inductance and capacitance as

$$\frac{dX(\omega_0)}{d\omega_0} = \frac{1}{\omega_0^2 C_s} + L_s \quad (20)$$

Solving equations (19) and (20) gives the following solutions for the series LC circuit elements

$$L_s = \frac{X(\omega_0) + \omega_0 X'(\omega_0)}{2\omega_0} \quad (21)$$

$$C_s = \frac{-2}{\omega_0(X(\omega_0) - \omega_0 X'(\omega_0))} \quad (22)$$

For the parallel LC resonance case, expression for the inductance L_p and capacitance C_p can be found in the Appendix B.

To design a benchmark narrowband structure, we work directly with a realistic structure to match a certain phase requirement in a single frequency. This is equivalent to changing L and C values to match certain impedance (Eq. 19) but not its derivative (Eq. 20). More details of the design procedure are explained in Sec. III A. Here, we show the extracted L and C values from the narrowband design and its phase profile for comparisons. As shown in Fig. 7(a), by appropriately tailoring the series or parallel resonance according to the broadband dispersive design, the phase from the calculated transmission line model (continuous curve) matches the designed phase profile (dashed curve). However, the phase obtained by the narrowband approach as in Fig. 7(b), matches the design only at the center frequency. To decide whether to use an LC resonant configuration in series or parallel, we evaluate whether a pole or a zero is closest to the center frequency. An example of this is depicted in Fig. 7(c). Here, the

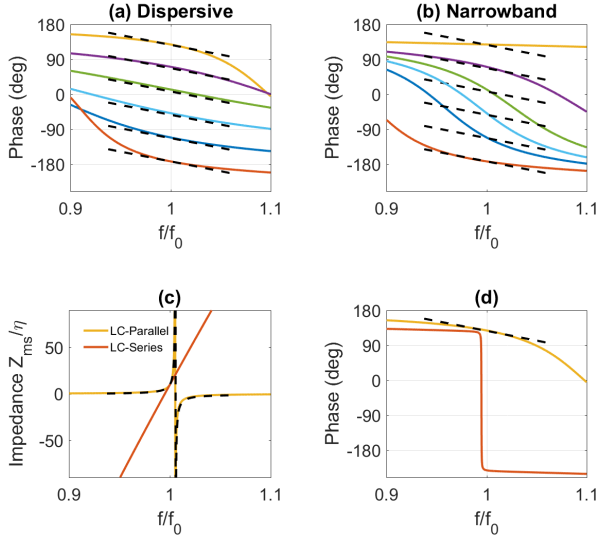


FIG. 7. Reflection phase for six unit cells of the broadband dispersive metasurface. (a) fitting both the impedance and its derivative and (b) fitting only the impedance (narrowband approach). The dashed lines show the target values, the solid lines show the fitted values. (c) Comparison of the series and parallel fits to the impedance for one cell of the metasurface, along with (d) the corresponding reflection phase.

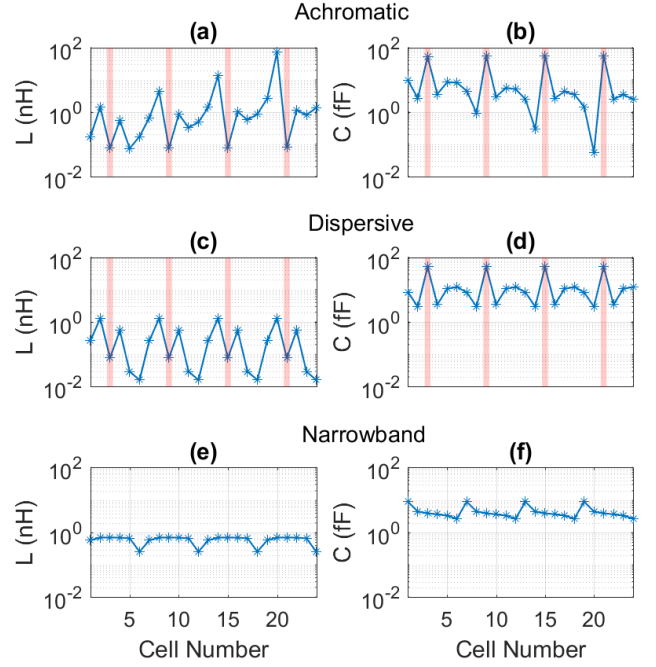


FIG. 8. Required inductance and capacitance values (on a log-scale) for different locations across each metasurface. (a,b) Broadband achromatic design, (c,d) broadband dispersive design, (e,f) narrowband design. The red shading indicates a cell with a parallel LC circuit implementation, the remainder cells are implemented using a series LC circuit.

pole is near the center frequency (f_0), thus fitting to a series resonance, even with both impedance and its derivative considered, gives an incorrect broadband profile, as shown by the red curve. The reflection phase depicted in Fig. 7(d) shows a large discrepancy between the designed phase (dashed curve) and its LC-series fitting (red curve). A LC-parallel implementation gives better fitting to both the impedance and reflection phase as depicted by the yellow curves in Fig. 7(c) and (d).

In Fig. 8, we show the fitted inductance and capacitance for a broadband achromatic metasurface (a,b), compared to the broadband dispersive (c,d) and the narrowband case (e,f). We use a similar design profile from Section II B with period of $X=7.8$ mm and six meta-atoms per super-cell for the periodic designs (meta-atom lateral size=1.3 mm). Meta-atoms which require LC-parallel circuits for their realizations are indicated by the red shading. We see that for the achromatic metasurface, the required LC values are not periodic. For distances further from the center of the metasurface, the inductance increases while the capacitance decreases. For both inductance and capacitance, the ratio between the smallest and largest values exceeds 10^3 . This makes achromatic metasurfaces with a large aperture very difficult to realize, since fabrication tolerances and available space within each meta-atom's cell will limit the achievable values of inductance and capacitance. In the broadband dispersive metasurface, the required LC values are periodic, with maximum ratio between the smallest and the largest is below 10^2 . In principle, this will make the

broadband dispersive metasurface much easier to realize than the broadband achromatic. In the narrowband case, since the derivative of impedance is not taken into account, only small changes in either inductance or capacitance are needed, as depicted in Fig. 8(e,f). We will show in the next section that this can be realized by changing only one geometrical parameter of a particular metallic structure.

In Section II B we noted that the broadband design procedure used a fixed value of Z_o at all frequencies, despite the frequency dependent refraction angle. We have repeated the design procedure using frequency dependent Z_o , and found that the required L and C for the dispersive metasurface case change by less than 2.5%. This difference is within the fabrication tolerance of the manufacturing process outlined below, and neglecting this term simplifies the design process, as well as the limit presented in Eq. (18).

III. NUMERICAL AND EXPERIMENTAL VERIFICATION

A. Meta Atom Design

Our strategy to implement the series and parallel LC resonances is to create simple metallic structures analogous to these circuit. In this work, we use a dog-bone structure for the series LC resonances and an inverse dog-bone structure for the parallel resonances. The dog-bone structure is an anisotropic capacitively loaded dipole [38, 39], whereas the inverse dog-bone structure is an inductive grid with a small metallic inclusion [40]. Using a homogenous approximation, the difference between the two simple structures can be explained as dipole resonances in a transparent or opaque medium [41]. Both of these structures can be tailored to have impedance suitable for broadband metasurfaces.

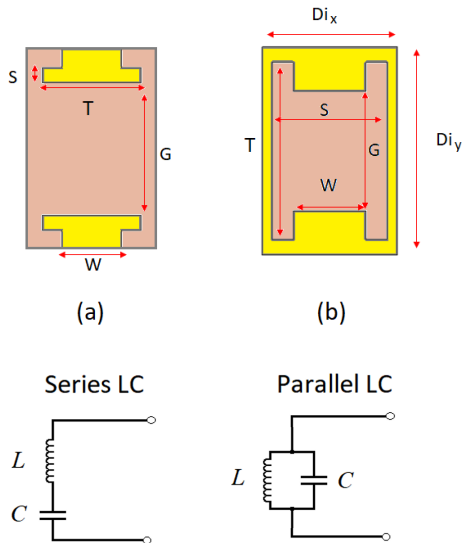


FIG. 9. Metasurface unit cell realization: (a) dog-bone structure, having a series LC resonance (b) inverse dog-bone structure, having a parallel LC resonance.

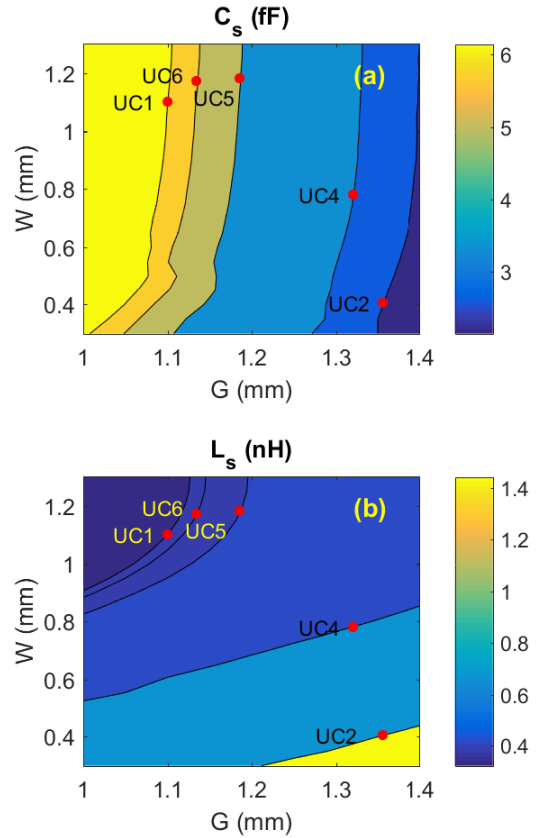


FIG. 10. (a) Capacitance and (b) inductance, extracted from the dog-bone structure using numerical simulation with varying parameter G and W . Red dots indicate the chosen dog-bone implementation.

Fig. 9(a) shows the dog-bone structure corresponding to the series LC realization. When illuminated by a vertically polarized wave, we see that the capacitance is provided by the metallic bars with length T and gap G . This capacitive element is connected in series by an inductive element of width W , which bridges both metallic bars. Shown in Fig. 9(b), the inverse dog-bone structure will exhibit a parallel LC resonance when illuminated by vertically polarized waves. The inductive element comes from the conducting bar with length T , and the capacitive element comes from the plates having a width of W and a separation of G . Analytical formulas exist for both structures, relating L and C values to geometrical parameters [42, 43]. However, due to the presence of near-field coupling between the dog-bones and metallic ground-plane [29, 44], such formulas were not found to be accurate. Therefore, a full-wave simulation has been performed, using a parametric sweep to obtain a lookup table.

Simulations are performed using the frequency domain solver of CST Microwave Studio [45]. To calculate the response of each structure we use a locally homogeneous approximation, based on unit-cell boundary conditions. From the reflection parameters, we calculate the effective metasurface impedance Z_{surf} using Eq. (4). We then implement Eq. (7) in a post-processing procedure to extract Z_{ms} automatically from each simulation run. In this way, we obtain

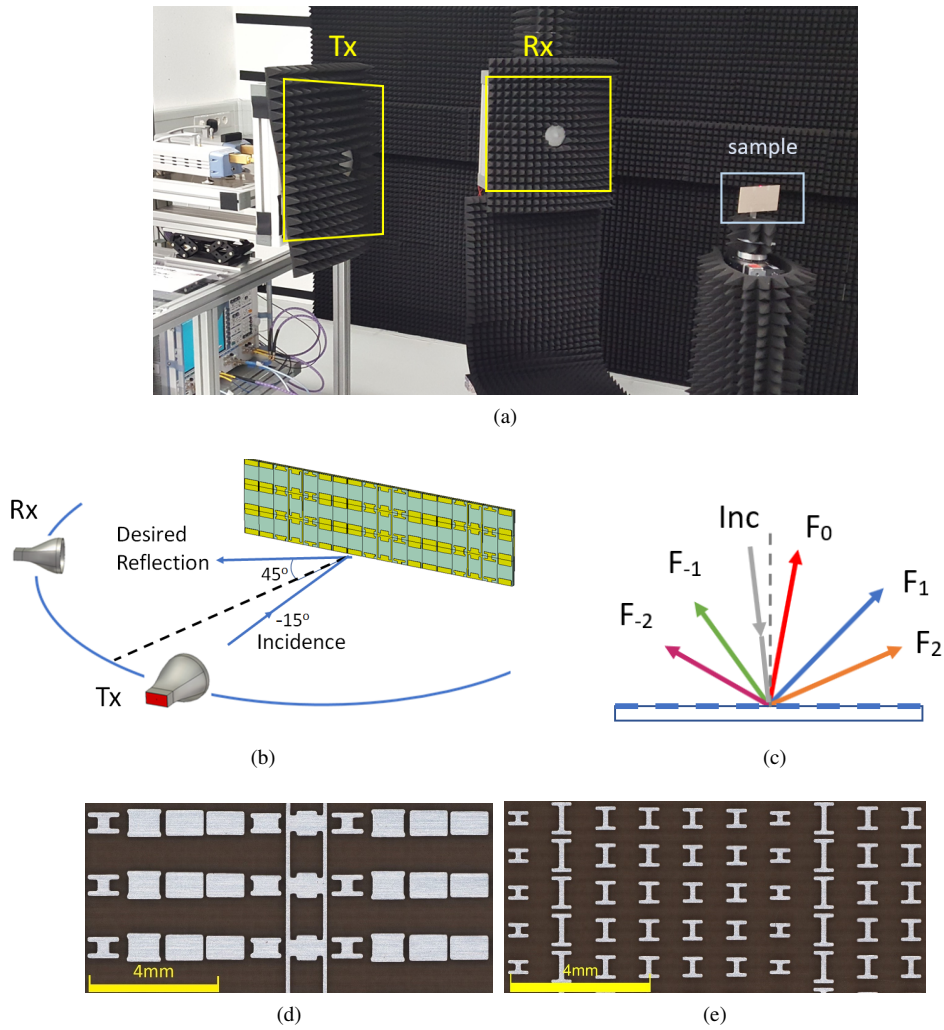


FIG. 11. (a) Photograph of the measurement setup. (b) Illustration of bi-static measurement with transmitter (Tx) and receiver (Rx) arms. (c) Schematic of all Floquet harmonics used in the measurement. (d) Zoomed photograph of the broadband dispersive metasurface sample. (e) Zoomed photograph of the narrowband metasurface sample.

the impedance Z_{ms} as well as its derivative at the operating frequency $f_0 = 80$ GHz and can calculate inductance and capacitance according to Eq. (21) and (22). Fig. 10 (a) and (b) depicts how the dog-bone structure parameters G and W determine the extracted capacitance (C_s) and inductance (L_s). The highlighted contour plots indicate capacitance and inductance suitable for the broadband dispersive design. The chosen W and G values for the corresponding unit cell implementations are indicated by red-dots and labeled by unit cell number (UCn). From both figures, we see that minimum obtainable capacitance is slightly below 1 fF, and maximum obtainable inductance is around 1.4 nH. Although these values are within the range for the broadband dispersive design, as shown in Fig. 8 (a,b), they do not cover the required inductance and capacitance of the achromatic design, even for a relatively small aperture (around 18 cells). Therefore, we only attempt to realize the broadband dispersive metasurface and the narrowband metasurface, in which the narrowband metasurfaces serves as a reference.

The narrowband design is implemented by changing the gap G , to modify capacitance and inductance in accordance with Fig. 8 (e, f). As can be seen from Fig. 10 (a, b), a geometrical sweep of G drastically changes the extracted capacitance and slightly changes the extracted inductance. Whereas a geometrical sweep of W has very small influence on the capacitance. Therefore, one geometrical sweep of G is enough to fit inductance and capacitance requirement of the narrowband metasurface implementation, especially with only small variation required for the inductance value as shown by Fig. 8 (e). The complete geometrical parameters for the broadband dispersive and narrowband metasurfaces are shown in the Appendix C.

B. Numerical and Experimental Verification

To verify the design procedure, we fabricate metasurface samples for operation within the W-band (75-110 GHz) and

measure their far-field responses. We use standard commercial printed circuit board (PCB) processing with an etching resolution of $100\ \mu\text{m}$ to fabricate the samples. The substrate is Isola ASTRA MT77 which has a dielectric constant of 3, a dissipation factor of 0.0017 and a thickness of $254\ \mu\text{m}$. Both metallic layers are copper, with a thickness of $18\ \mu\text{m}$. The overall sample sizes are $100\ \text{mm} \times 55\ \text{mm}$. Both, the broadband dispersive and the narrowband designs were fabricated and a microscopy photograph of a sample of each design is shown in Fig. 11(d) and (e), respectively.

A bi-static measurement setup [46, 47] operating at W-band is used to characterize the metasurface samples, as shown in Fig. 11(a) and (b). The receiver arm (Rx) can move on a circle with a radius of 1 meter and the bistatic angle can be varied from 25° to 335° . There is a blind range of 50° , since the antennas cannot overlap each other. The rotation has 0.1° precision, controlled automatically by an external computer which also collects measurement data from the Vector Network Analyzer (VNA). The propagating Floquet harmonics which may be reflected from the metasurface are illustrated in Fig. 11(b), and all of these were measured. The procedure involves four runs of far-field measurement, with four different incident angles as shown in Table I. These incident angles were chosen to account for the blind angular range, ensuring that the specular reflection and other Floquet harmonics were well captured by the measurement system. Additionally, Fabry-Perot resonances between the sample and exciting antenna were avoided by using these non-normal incident angles. From the far-field measurement data, we extract the intensity of individual Floquet harmonics as per the procedure described in [47].

TABLE I. Different incident angles used to measure all possible Floquet harmonics from the metasurface

Run	θ_{in}	Floquet Mode
1	-15	F_0, F_1
2	-5	F_2
3	5	F_{-2}
4	15	F_{-1}

The measured Floquet harmonics are plotted in Fig. 12(a) and (b) for the broadband dispersive and narrowband metasurfaces respectively. The results are normalized to reflection spectra from a metallic mirror having the same size as the metasurfaces ($110 \times 55\ \text{mm}$). We run a full-wave simulation using CST Microwave Studio [45] and the results for the specular reflection (F_0) and the desired diffraction order (F_1) are plotted as dotted lines. The metasurfaces were designed for 80 GHz center frequency, however, we observe that the spectra are shifted by around 2 GHz due to fabrication tolerances. The simulation results plotted in Fig. 12 were calculated with the patterned metallic layer scaled by 0.976 in the x and y axes, in order to have a good match with measurement results.

Measurements of both structures show that the dominant mode is the desired +1 diffraction order (F_1). However, the broadband design has a more stable power spectrum, maintaining a higher received power in a larger bandwidth. For the narrowband design, we observed a faster reduction in power

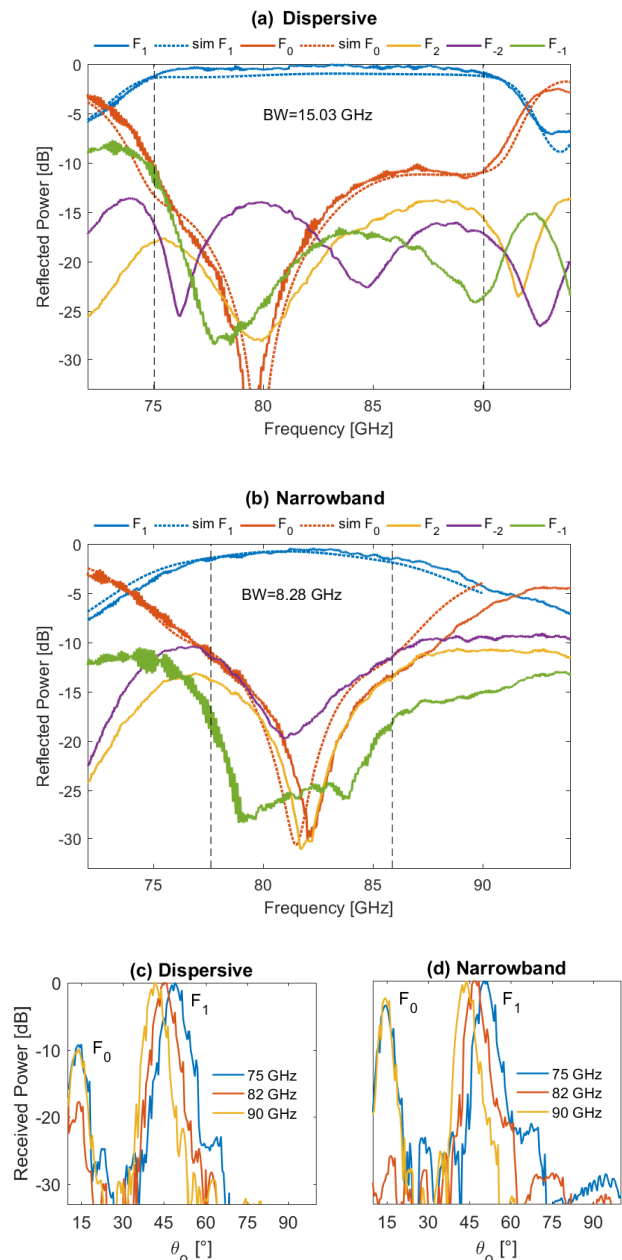


FIG. 12. All propagating Floquet harmonics measured over the frequency range of 72-94 GHz for (a) the broadband dispersive metasurface, (b) the narrowband metasurface. Simulation results from specular reflection (F_0) and the desired diffraction order (F_1) are plotted with a dotted-line. Far field measurement results of F_0 and F_1 from (c) the broadband dispersive metasurface and (d) the narrowband metasurface for three different frequencies.

of the F_1 mode as the frequency shifts further away from the center. Additionally, the narrowband design has a faster increase of undesired diffraction orders (F_0 and F_{-2}) away from the center frequency, which can compromise the anomalous reflection performance. We calculate the bandwidth over which the desired reflection spectra is above -3 dB, with minimum 10 dB difference to other diffraction modes. In the broadband design, the bandwidth is 15.03 GHz correspond-

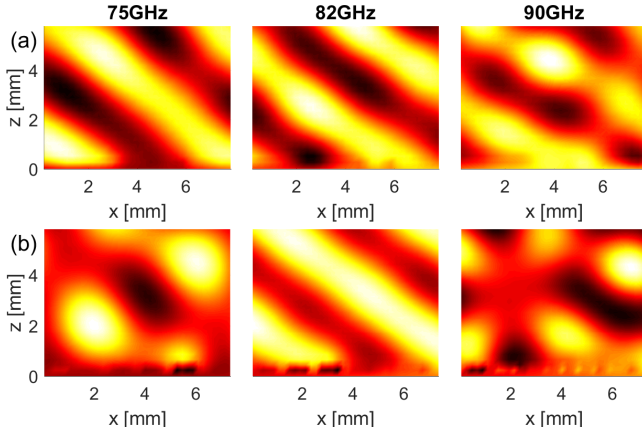


FIG. 13. Scattered near field-simulation results (real part of electric field) for broadband dispersive metasurface (a) and narrowband metasurface (b) in three different frequencies.

ing to a fractional bandwidth of $\delta=18.22\%$, whereas in the narrowband design the bandwidth is 8.28 GHz corresponding to a fractional bandwidth of $\delta=9.98\%$.

The measured far-field pattern of the broadband dispersive and narrowband metasurfaces are plotted in Fig. 12(c)-(d) for three different frequencies. Each measurement is normalized to its peak value. Here, the incident angle is -15° and the desired diffraction order is $\theta_o = 45^\circ$. The measured peak of F_1 in the center frequency (82 GHz) indeed showed they are at 45° . The specular reflection peaks are at 15° and are indicated by F_0 . From the broadband dispersive measurement results we see that they are equal to or below 10 dB at all frequencies, whereas the narrowband metasurface fails to suppress the specular reflections to below 10 dB difference at 75 and 90 GHz. To further illustrate these results, the electric field within the supercell of the full-wave simulations is plotted in Fig. 13(a) and (b), for these same three frequencies. In the broadband dispersive metasurface, the dominant reflection for all three frequencies is the F_1 mode, exceeding other modes by 10 dB. Thus, we see that the incident plane wave is smoothly reflected into the desired angle with comparatively little interference. However, from the narrowband metasurface, the specular reflection at 75 and 90 GHz has only around 3 dB difference to the desired diffraction order, causing strong interference and non-ideal anomalous reflections.

IV. CONCLUSION

We developed and experimentally verified a synthesis procedure which enables the realization of broadband anomalous reflection using metasurfaces. We showed that two scenarios may appear to realize broadband anomalous reflection, either

using an achromatic or a dispersive approach. In the dispersive approach, a metasurface can be made broadband without varying group delay across its lateral dimension, allowing an easier implementation procedure. We analyzed the role of additional group delay and showed that it is directly related to the realizability of passive broadband impedances. In realizing the broadband impedance, the required meta-atom layer impedance is fitted over a broad bandwidth using either a series or parallel configuration of LC resonances. The systematic procedure to obtain L and C elements for the meta-atoms is demonstrated, in which they are translated into realistic structures using dog-bone or inverse dog-bone structures. We verified the proposed method experimentally at millimeter-wave frequencies. The broadband dispersive metasurface achieves more than 90% increase of bandwidth compared to the narrowband design, with 10 dB contrast between the desired diffraction order and all other spurious orders. Since the presented procedure to obtain broadband impedance is generic, it allows the implementation of other wave-front manipulation functions and is applicable to other planar metallic meta-atom geometries, including those suited for terahertz and infrared wavelengths.

ACKNOWLEDGMENTS

This work was financially supported by the Australian Research Council (Linkage Project LP160100253), the Luxembourg Ministry of the Economy (grant CVN 18/17/RED), the University of New South Wales (UIPA scholarship) and the Indonesia Endowment Fund for Education (LPDP) (PRJ-1081/LPDP.3/2017).

Appendix A: Condition for realizable impedances

The impedance Z_{ms} of the patterned metallic layer must be compliant with Foster's reactance theorem, i.e. the imaginary part must increase with frequency. For the broadband dispersive case, substituting Eq. (1) into Eq. (10) yields

$$Z_{ms} = \frac{Z_o Z_s \tan(\omega t_s) \cot(\frac{\pi x}{X} + \frac{\omega t_o}{2})}{j Z_s \tan(\omega t_s) + j Z_o \cot(\frac{\pi x}{X} + \frac{\omega t_o}{2})}. \quad (A1)$$

The equation consists of four ω functions including two cotangent and tangent functions in the numerator and denominator. We notice that the derivative over frequency (ω) is a quotient and product rule problem in which each of the implementing operation requires the use of chain rules. We applied this to Eq. (A1) and after substituting cotangent to tangent, we have,

$$\frac{dZ_{ms}}{d\omega} = \frac{Z_o Z_s \left(\frac{2Z_o t_s}{\cos^2(\omega t_s)} - \frac{2Z_o t_s}{\sin^2(\frac{\pi x}{X} + \frac{\omega t_o}{2}) \cos^2(\omega t_s)} - \frac{Z_s t_o}{\sin^2(\frac{\pi x}{X} + \frac{\omega t_o}{2})} + \frac{Z_s t_o}{\sin^2(\frac{\pi x}{X} + \frac{\omega t_o}{2}) \cos^2(\omega t_s)} \right) \tan^2(\frac{\pi x}{X} + \frac{\omega t_o}{2})}{2(Z_o + Z_s \tan(\omega t_s) \tan(\frac{\pi x}{X} + \frac{\omega t_o}{2}))^2} \quad (A2)$$

Since we want to know the condition for $\frac{dZ_{ms}}{d\omega} = 0$, we seek the zeros of the numerator (having confirmed there is no contribution from poles on the denominator). After simplifying, we have

$$2Z_o t_s \sin^2 \left(\frac{\pi x}{X} + \frac{\omega t_0}{2} \right) - 2Z_o t_s - Z_s t_0 \cos^2(\omega t_s) + Z_s t_0 = 0 \quad (\text{A3})$$

Applying the identity $\sin^2 x + \cos^2 x = 1$, we have

$$-2Z_o t_s \cos^2 \left(\frac{\pi x}{X} + \frac{\omega t_0}{2} \right) + Z_s t_0 \sin^2(\omega t_s) = 0. \quad (\text{A4})$$

Simplifying Eq. (A4) leads to Eq. (16)

For the broadband achromatic case, substituting Eq. (3) into Eq. (10) yields

$$Z_{ms} = \frac{Z_o Z_s \tan(\omega t_s) \cot(\omega(\frac{\Delta\theta x}{2c} + \frac{t_0}{2}))}{jZ_s \tan(\omega t_s) + jZ_o \cot(\omega(\frac{\Delta\theta x}{2c} + \frac{t_0}{2}))}. \quad (\text{A5})$$

Repeating the same process for finding its derivative and equating it to zero, we have

$$-2Z_o t_s \cos^2 \left(\frac{\omega \Delta\theta x}{2c} + \frac{\omega t_0}{2} \right) + Z_s \left(\frac{\Delta\theta x}{c} + t_0 \right) \sin^2(\omega t_s) = 0 \quad (\text{A6})$$

Simplifying Eq. (A6) leads to Eq. (17).

Appendix B: Parallel LC Approximation

If the meta-atom layer impedance Z_{ms} has a pole within the design bandwidth, it will be best fitted by a parallel LC circuit. By expressing the reactance as a susceptance ($B_{ms} = -\frac{1}{X_{ms}}$) the poles are transformed into zeros, and the susceptance is fitted to LC parameters using its value and derivative at the center frequency, similar as the LC series.

$$B = \omega C_p - \frac{1}{\omega L_p} \quad (\text{B1})$$

$$\frac{dB}{d\omega} = \frac{1}{\omega^2 L_p} + C_p \quad (\text{B2})$$

Solving these equations leads to the following expressions for the inductance and capacitance

$$C_p = \frac{B(\omega_0) + \omega_0 B'(\omega_0)}{2\omega_0} \quad (\text{B3})$$

$$L_p = \frac{-2}{\omega_0(B(\omega_0) - \omega_0 B'(\omega_0))} \quad (\text{B4})$$

Shown in Fig. 14(a) is the imaginary part of admittance (dotted line), taken from one of the meta-atoms explained in subsection II B. The linear function is fitted using LC-parallel elements and the result is shown by the blue line. This linear function has a zero near to the center frequency, equivalent to a pole in its impedance expression shown in Fig. 14(b).

Appendix C: Meta-atom Parameters

After simulating the dog-bone and inverse dog-bone geometrical parameter sweep using CST, a look-up table containing extracted inductance and capacitance values was created. Based on the match to the required L and C, six geometrical combinations for the meta-atom implementation were chosen. Table. II shows detail of the realized dog-bone and inverse dog-bone structure for the broadband dispersive metasurface. Here, unit cell no. 3 is implemented using an inverse dog-bone structure (parallel LC), while the rest are implemented using dog-bone structures (series LC). Note, that the initial look-up table shown by Fig. 10(a, b) is using $T=1.2\text{mm}$ and $S=0.15\text{mm}$. In several meta-atoms, the parameter T has been adjusted to account for the rounding effects (due to the etching resolution in fabrication).

TABLE II. Dog-bone and inverse dog-bone geometrical parameters (in millimeters) for the broadband dispersive metasurface implementation

Cell No.	G	W	T	S
1	1.10	1.00	1.10	0.15
2	1.32	0.36	1.00	0.15
3*	1.20	1.05	1.50	0.20
4	1.35	0.80	1.00	0.15
5	1.24	1.20	1.20	0.15
6	1.17	1.20	1.20	0.15

TABLE III. Dog-bone geometrical parameters (in millimeters) for the narrowband metasurface implementation

Cell No.	G	W	T	S
1	0.14	0.15	0.60	0.10
2	0.40	0.15	0.60	0.10
3	0.45	0.15	0.60	0.10
4	0.48	0.15	0.60	0.10
5	0.52	0.15	0.60	0.10
6	0.67	0.15	0.60	0.10

For the narrowband metasurface, the meta-atom implementation only requires one geometrical sweep from the dog-bone

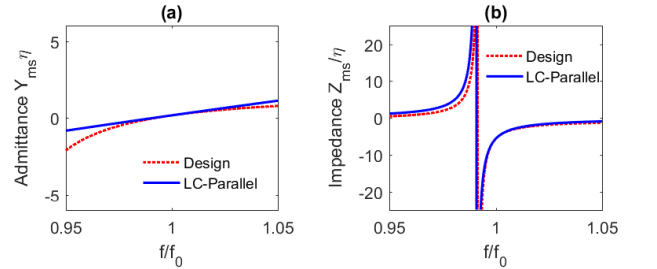


FIG. 14. (a) Imaginary part of the design admittance Y_{ms} (red-dotted line) and the calculated parallel-LC fitting results (blue line). (b) Equivalent metasurface design impedance Z_{ms} (red-dotted line) and the calculated fitting results (blue line).

structure. The chosen combinations for narrowband meta-atoms are shown in Table. III. The vertical size of the meta

atom in this narrowband design is $D_y=1.08$ mm, while for the broadband dispersive design it is $D_y=2$ mm.

-
- [1] S. Maci, G. Minatti, M. Casaletti, and M. Bosiljevac, Meta-surfing: Addressing waves on impenetrable metasurfaces, *IEEE Antennas and Wireless Propagation Letters* **10**, 1499 (2011).
- [2] X. Ni, N. K. Emani, A. V. Kildishev, A. Boltasseva, and V. M. Shalaev, Broadband light bending with plasmonic nanoantennas, *Science* **335**, 427 (2012).
- [3] A. Pors, O. Albrektsen, I. P. Radko, and S. I. Bozhevolnyi, Gap plasmon-based metasurfaces for total control of reflected light, *Scientific reports* **3**, 2155 (2013).
- [4] S. Sun, K.-Y. Yang, C.-M. Wang, T.-K. Juan, W. T. Chen, C. Y. Liao, Q. He, S. Xiao, W.-T. Kung, G.-Y. Guo, *et al.*, High-efficiency broadband anomalous reflection by gradient metasurfaces, *Nano letters* **12**, 6223 (2012).
- [5] X. Chen, L. Huang, H. Mühlenbernd, G. Li, B. Bai, Q. Tan, G. Jin, C.-W. Qiu, S. Zhang, and T. Zentgraf, Dual-polarity plasmonic metalens for visible light, *Nature communications* **3**, 1198 (2012).
- [6] A. Pors, M. G. Nielsen, R. L. Eriksen, and S. I. Bozhevolnyi, Broadband focusing flat mirrors based on plasmonic gradient metasurfaces, *Nano letters* **13**, 829 (2013).
- [7] Y. Zárate, I. V. Shadrivov, and D. A. Powell, Tunable focusing by a flexible metasurface, *Photonics and Nanostructures-Fundamentals and Applications* **26**, 62 (2017).
- [8] Y. Yang, W. Wang, P. Moitra, I. I. Kravchenko, D. P. Briggs, and J. Valentine, Dielectric meta-reflectarray for broadband linear polarization conversion and optical vortex generation, *Nano letters* **14**, 1394 (2014).
- [9] X. Ma, M. Pu, X. Li, C. Huang, Y. Wang, W. Pan, B. Zhao, J. Cui, C. Wang, Z. Zhao, *et al.*, A planar chiral meta-surface for optical vortex generation and focusing, *Scientific reports* **5**, 10365 (2015).
- [10] S. Sun, Q. He, S. Xiao, Q. Xu, X. Li, and L. Zhou, Gradient-index meta-surfaces as a bridge linking propagating waves and surface waves, *Nature materials* **11**, 426 (2012).
- [11] C. Qu, S. Xiao, S. Sun, Q. He, and L. Zhou, A theoretical study on the conversion efficiencies of gradient meta-surfaces, *EPL (Europhysics Letters)* **101**, 54002 (2013).
- [12] V. Asadchy, M. Albooyeh, S. Tsvetkova, A. Díaz-Rubio, Y. Ra'di, and S. Tretyakov, Perfect control of reflection and refraction using spatially dispersive metasurfaces, *Physical Review B* **94**, 075142 (2016).
- [13] A. Díaz-Rubio, V. S. Asadchy, A. Elsakka, and S. A. Tretyakov, From the generalized reflection law to the realization of perfect anomalous reflectors, *Science advances* **3**, e1602714 (2017).
- [14] S. Larouche and D. R. Smith, Reconciliation of generalized refraction with diffraction theory., *Optics letters* **37**, 2391 (2012).
- [15] E. Arbabi, A. Arbabi, S. M. Kamali, Y. Horie, and A. Faraon, Multiwavelength metasurfaces through spatial multiplexing, *Scientific reports* **6**, 32803 (2016).
- [16] Z. Shi, M. Khorasaninejad, Y.-W. Huang, C. Roques-Carnes, A. Y. Zhu, W. T. Chen, V. Sanjeev, Z.-W. Ding, M. Tamagnone, K. Chaudhary, *et al.*, Single-layer metasurface with controllable multiwavelength functions, *Nano letters* **18**, 2420 (2018).
- [17] Z. Li, E. Palacios, S. Butun, and K. Aydin, Visible-frequency metasurfaces for broadband anomalous reflection and high-efficiency spectrum splitting, *Nano letters* **15**, 1615 (2015).
- [18] S. Gao, S.-S. Lee, E.-S. Kim, and D.-Y. Choi, Vertically integrated visible and near-infrared metasurfaces enabling an ultra-broadband and highly angle-resolved anomalous reflection, *Nanoscale* **10**, 12453 (2018).
- [19] X. You, R. T. Ako, W. S. L. Lee, M. X. Low, M. Bhaskaran, S. Sriram, C. Fumeaux, and W. Withayachumnankul, Terahertz reflectarray with enhanced bandwidth, *Advanced Optical Materials* **7**, 1900791 (2019).
- [20] F. Callewaert, V. Velev, P. Kumar, A. Sahakian, and K. Aydin, Inverse-designed broadband all-dielectric electromagnetic metadevices, *Scientific reports* **8**, 1358 (2018).
- [21] E. Arbabi, A. Arbabi, S. M. Kamali, Y. Horie, and A. Faraon, Controlling the sign of chromatic dispersion in diffractive optics with dielectric metasurfaces, *Optica* **4**, 625 (2017).
- [22] M. Khorasaninejad, Z. Shi, A. Y. Zhu, W.-T. Chen, V. Sanjeev, A. Zaidi, and F. Capasso, Achromatic metalens over 60 nm bandwidth in the visible and metalens with reverse chromatic dispersion, *Nano letters* **17**, 1819 (2017).
- [23] S. Shrestha, A. C. Overvig, M. Lu, A. Stein, and N. Yu, Broadband achromatic dielectric metalenses, *Light: Science & Applications* **7**, 85 (2018).
- [24] S. Wang, P. C. Wu, V.-C. Su, Y.-C. Lai, C. H. Chu, J.-W. Chen, S.-H. Lu, J. Chen, B. Xu, C.-H. Kuan, *et al.*, Broadband achromatic optical metasurface devices, *Nature communications* **8**, 187 (2017).
- [25] Q. Cheng, M. Ma, D. Yu, Z. Shen, J. Xie, J. Wang, N. Xu, H. Guo, W. Hu, S. Wang, *et al.*, Broadband achromatic metalens in terahertz regime, *Science Bulletin* (2019).
- [26] Y. Huang, M. Pu, F. Zhang, J. Luo, X. Li, X. Ma, and X. Luo, Broadband functional metasurfaces: Achieving nonlinear phase generation toward achromatic surface cloaking and lensing, *Advanced Optical Materials* , 1801480 (2019).
- [27] M. Li, M. A. Al-Joumayly, and N. Behdad, Broadband true-time-delay microwave lenses based on miniaturized element frequency selective surfaces, *IEEE Transactions on Antennas and Propagation* **61**, 1166 (2012).
- [28] A. A. Fathman and D. A. Powell, Bandwidth and size limits of achromatic printed-circuit metasurfaces, *Optics express* **26**, 29440 (2018).
- [29] A. E. Olk and D. A. Powell, Accurate metasurface synthesis incorporating near-field coupling effects, *Physical Review Applied* **11**, 064007 (2019).
- [30] N. Yu, P. Genevet, M. A. Kats, F. Aieta, J.-P. Tetienne, F. Capasso, and Z. Gaburro, Light propagation with phase discontinuities: generalized laws of reflection and refraction, *science* **334**, 333 (2011).
- [31] B. Sima, K. Chen, X. Luo, J. Zhao, and Y. Feng, Combining frequency-selective scattering and specular reflection through phase-dispersion tailoring of a metasurface, *Physical Review Applied* **10**, 064043 (2018).
- [32] F. Aieta, M. A. Kats, P. Genevet, and F. Capasso, Multiwavelength achromatic metasurfaces by dispersive phase compensation, *Science* **347**, 1342 (2015).
- [33] A. Epstein and G. V. Eleftheriades, Huygens metasurfaces via the equivalence principle: design and applications, *JOSA B* **33**, A31 (2016).
- [34] R. M. Foster, A reactance theorem, *Bell Labs Technical Journal* **3**, 259 (1924).

- [35] M. Kara, A simple technique for the calculation of the bandwidth of rectangular microstrip antenna elements with various substrate thicknesses, *Microwave and Optical Technology Letters* **12**, 16 (1996).
- [36] Ş. Sağıroğlu, K. Güney, and M. Erler, Calculation of bandwidth for electrically thin and thick rectangular microstrip antennas with the use of multilayered perceptrons, *International Journal of RF and Microwave Computer-Aided Engineering* **9**, 277 (1999).
- [37] Y. Zhao and A. Alu, Tailoring the dispersion of plasmonic nanorods to realize broadband optical meta-waveplates, *Nano letters* **13**, 1086 (2013).
- [38] C. Pfeiffer and A. Grbic, Millimeter-wave transmitarrays for wavefront and polarization control, *IEEE Transactions on Microwave Theory and Techniques* **61**, 4407 (2013).
- [39] B. A. Munk, *Frequency Selective Surfaces: Theory and Design* (John Wiley & Sons, New York, 2000).
- [40] C. L. Holloway and E. F. Kuester, Generalized sheet transition conditions for a metascreen—a fishnet metasurface, *IEEE Transactions on Antennas and Propagation* **66**, 2414 (2018).
- [41] B. Yang, T. Liu, H. Guo, S. Xiao, and L. Zhou, High-performance meta-devices based on multilayer meta-atoms: interplay between number of layer and phase coverage, *Science Bulletin* (2019).
- [42] O. Luukkonen, C. Simovski, G. Granet, G. Goussetis, D. Lioubtchenko, A. V. Raisanen, and S. A. Tretyakov, Simple and accurate analytical model of planar grids and high-impedance surfaces comprising metal strips or patches, *IEEE Transactions on Antennas and Propagation* **56**, 1624 (2008).
- [43] H. L. Liu, K. L. Ford, and R. J. Langley, Design methodology for a miniaturized frequency selective surface using lumped reactive components, *IEEE Transactions on Antennas and Propagation* **57**, 2732 (2009).
- [44] H. Tao, C. Bingham, A. Strikwerda, D. Pilon, D. Shrekenhamer, N. Landy, K. Fan, X. Zhang, W. Padilla, and R. Averitt, Highly flexible wide angle of incidence terahertz metamaterial absorber: Design, fabrication, and characterization, *physical review B* **78**, 241103 (2008).
- [45] CST Microwave Studio 2019, Darmstadt, Germany.
- [46] A. Olk, K. B. Khadhra, and T. Spielmann, Highly accurate fully-polarimetric radar cross section facility for mono- and bistatic measurements at w-band frequencies, in *2017 Antenna Measurement Techniques Association Symposium (AMTA)* (IEEE, 2017) pp. 1–6.
- [47] A. E. Olk, P. E. Macchi, and D. A. Powell, Experimental characterization of refracting millimeter-wave metasurfaces, arXiv preprint arXiv:1910.06069 (2019).